Micron 201 (2026) 103960

Contents lists available at ScienceDirect

Micron

journal homepage: www.elsevier.com/locate/micron

Structure of metal-organic framework nanocrystals obtained from electron diffraction data by iterative phase retrieval

Tatiana E. Gorelik [a,b,*,1], Tatiana Latychevskaia [c,d,1], Irena Senkovska [e], Mariia Maliuta [e], Stefan Kaskel [e], Ute Kaiser [a]

[a] Ernst Ruska-Centre for Microscopy and Spectroscopy with Electrons, Forschungszentrum Jülich GmbH, Jülich 52428, Germany
[b] Ulm University, Central Facility of Electron Microscopy, Materials Science Electron Microscopy, Albert Einstein Allee 11, Ulm 89069, Germany
[c] Paul Scherrer Institute, Forschungsstrasse 111, Villigen 5232, Switzerland
[d] Physics Department, University of Zurich, Winterthurerstrasse 190, Zurich 8057, Switzerland
[e] Chair of Inorganic Chemistry I, Technische Universität Dresden, Bergstrasse 66, Dresden 01069, Germany

ARTICLE INFO

Keywords:
Electron diffraction
Nanocrystals
Iterative phase retrieval
Coherent diffraction Imaging
Metal-organic framework

ABSTRACT

We demonstrate the iterative phase retrieval of DUT-8(Ni) metal-organic framework (MOF) nanocrystals using high-resolution electron diffraction data. The reconstructed images show contrast features associated with the crystal structure, revealing well-resolved metal-containing rows with interpretable shifts. These shifts correspond to previously reported crystal structure disorder within the MOF. Furthermore, electron diffraction patterns display modulations in the low-resolution region, indicative of the rectangular crystal shape. Based on these data, we also successfully reconstructed the crystal shape image, which closely matched the observed form of the crystal.

1. Introduction

Extracting structural images directly from *electron diffraction patterns* offers several advantages, such as avoiding resolution compromise due to lens aberration and implementing a smart electron dose distribution for beam-sensitive materials. However, a fundamental challenge arises in the absence of phase information necessary for image reconstruction. *Coherent Diffraction Imaging (CDI)* (Miao et al., 1999) addresses this issue by employing an iterative phase retrieval algorithm (Gerchberg and Saxton, 1972; Fienup, 1982; Marchesini et al., 2003; Latychevskaia, 2018) on diffraction patterns to reconstruct the phase. The iterative algorithm involves propagating the wavefront back and forth between the sample and the detector planes, applying constraints in both planes, and iteratively finding the missing phases. The recovered sample structure is uniquely defined when the following conditions are met: the object under study is isolated, and the size of the reconstructed field of view exceeds the size of the object by at least twice in each direction (oversampling condition) (Miao et al., 1998). CDI has been successfully demonstrated with light, X-rays, electrons, and other waves. Although CDI is typically realized with X-rays, where no lenses are available, it has also been demonstrated for electrons. The superior resolution provided by CDI has been demonstrated by Zuo et al., who recovered the structure of a double-walled carbon nanotube (DWCNT) at atomic resolution from a diffraction pattern acquired using TEM with a nominal point resolution of 2.2 Å for normal imaging at the Scherzer focus conditions (Zuo et al., 2003). CDI is particularly challenging for imaging of nanocrystals, where the reconstructed structure can be non-uniquely defined (Wu et al., 2005). To solve this issue, any additional data that provides low-resolution information can serve as an initial model, allowing the diffraction pattern to enhance the high-resolution information of the reconstructed structure (Latychevskaia et al., 2012).

Electron ptychography has been demonstrated to achieve atomic resolution of 0.4 Å from a 4D-STEM dataset (Jiang et al., 2018) from a twisted bilayer MoS_2, which is known to be a material that can withstand relatively large radiation doses without significant radiation damage. Biological samples were imaged by electron ptychography at a resolution of 5 Å by placing the sample at a defocus that allowed to reduce the radiation dose (Zhou et al., 2020). In the experiments reported in this study, no beam scanning was employed, so that the sample structure was reconstructed from two single-shot intensity distributions:

* Corresponding author at: Ernst Ruska-Centre for Microscopy and Spectroscopy with Electrons, Forschungszentrum Jülich GmbH, Jülich 52428, Germany.
E-mail address: Tatiana.gorelik@uni-ulm.de (T.E. Gorelik).
[1] these authors contributed equally to this work.

https://doi.org/10.1016/j.micron.2025.103960
Received 7 March 2025; Received in revised form 11 November 2025; Accepted 17 November 2025
Available online 21 November 2025

the diffraction pattern of the crystal and the image of the crystal in the probe beam. This allowed to minimize the radiation dose during the first acquisition (diffraction pattern), making the approach potentially suitable for biological materials. We demonstrate what information about the sample structure can be recovered from these data.

For our study, we selected metal-organic framework (MOF) nanocrystals with a regular morphology. MOFs consist of inorganic building units, typically metal ions or metal clusters, interconnected by organic molecules (linkers) to form a framework. This architecture creates intrinsic voids, typically filled with solvent molecules used in the synthesis (Kaskel, 2016). Metal-containing vertices typically exhibit strong contrast and can be easily imaged in TEM, while the positions of organic linkers are often less resolved. MOFs, especially those able to change the crystal structure upon the influence of external stimuli such as adsorption/desorption of the guest molecules, often called flexible MOFs or soft porous crystals (Horike et al., 2009; Schneemann et al., 2014; Krause et al., 2020), are particularly interesting systems for TEM imaging, both for applications and methodological studies (Wiktor et al., 2017; Liu et al., 2020, Parent et al., 2017; Liu et al., 2019; Li et al., 2019).

The goal of this study is to compare structural information obtained for an electron beam-sensitive material through direct transmission electron microscopy TEM imaging (i) and by iterative reconstruction of diffraction patterns (ii).

2. Materials and methods

2.1. Synthesis of the sample

The $[Ni_2(ndc)_2(dabco)]_n$ nanocrystals (DUT-8(Ni), DUT – Dresden University of Technology) (Klein et al., 2010; Bon et al., 2015; Ehrling et al., 2021) were synthesised as described by Kavoosi et al. (2017). Ni $(NO_3)_2{\cdot}6\ H_2O$ (0.434 g, 1.50 mmol), 2,6-naphthalene dicarboxylic acid (H_2ndc) (0.294 g, 1.36 mmol), and 1,4-diazabicyclo-[2.2.2]-octane - dabco (0.336 g, 3.00 mmol) were mixed and sonicated in 30 mL of *N,N*-dimethylformamide (DMF) for 10 min. After mixing of all the chemicals, a cloudy suspension was obtained, which was transferred to a Teflon-lined autoclave, placed into a preheated oven at 408 K, and held at that temperature for 72 h. The resulting material was washed with 30 mL DMF twice and suspended in fresh DMF. The phase purity of the product obtained was proven by powder X-ray diffraction.

2.2. On the crystal structure of DUT-8(Ni)

DUT-8(Ni) consists of Ni-based dimers coordinated by four μ_2-bridging carboxylic groups (generally called paddle wheel building units), interconnected by 2,6-naphtalene into 2D layers. They are linked by 1,4-diazabicyclo-[2.2.2]-octane (dabco) by the coordination of the axial positions of the paddle wheels into a 3D framework (Senkovska et al., 2023). Two different regular crystal structures (polymorphs) are known for DUT-8(Ni) – polymorph A (tetragonal *P4/nmm*, CSD 1989709) and polymorph B (monoclinic *C2/m*, CSD 1989708) (Petkov et al., 2019). Fig. 1a shows a < 110 > projection of the tetragonal structure (green arrows indicate positions of nickel-dabco containing rows), Fig. 1b shows the corresponding projection of the monoclinic structure. The two crystal structures A and B differ in the relative orientation of the naphthalene linkers. Depending on the solvent present in the pores, crystals with different amounts of both structural fragments are produced (Ehrling et al., 2021). Fig. 1c shows a section of a disordered model, showing possible atomic arrangement in the real structure. The distance between the metal-containing rows is preserved and is equal to 13.0 Å, while the arrangement of atoms within the rows and the layers and their mutual shift differ. Since all layers can have individual atomic arrangements, their sequence cannot be regarded as stacking faults, being a special form of "*semi-crystalline*" order.

2.3. TEM data collection

Samples for TEM investigations were prepared by dropping the DMF

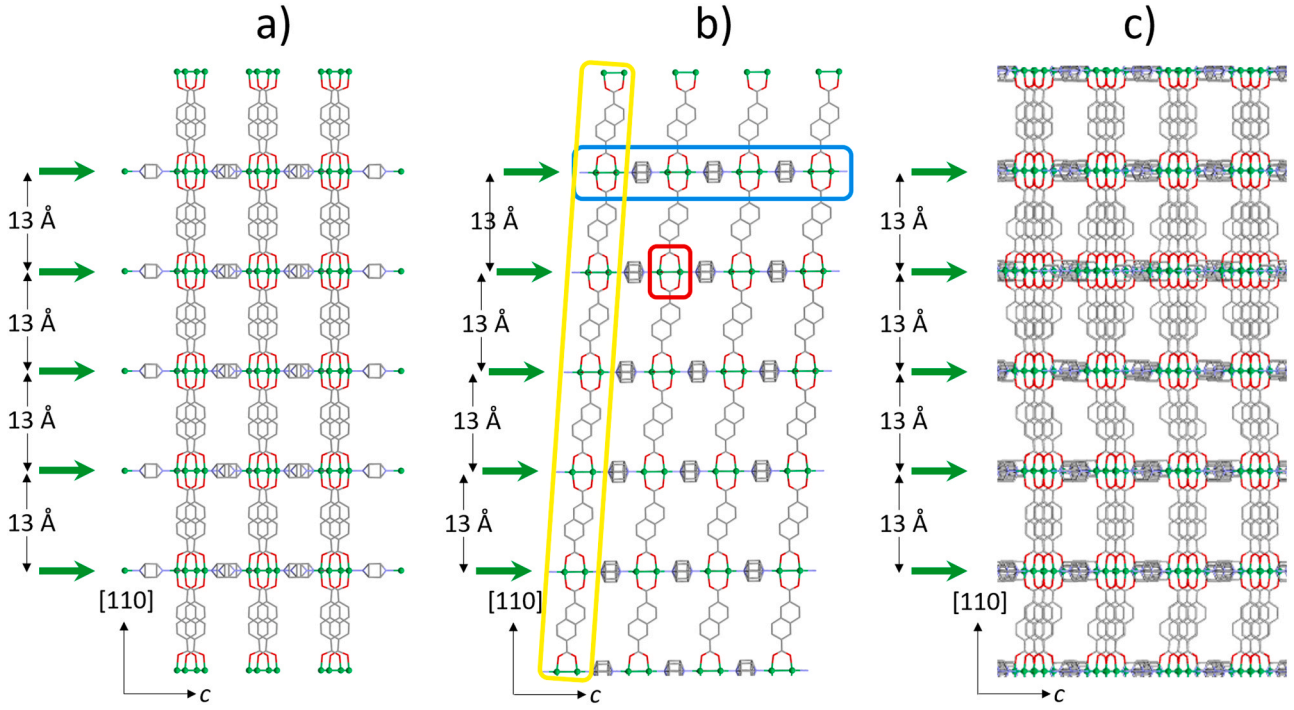

Fig. 1. DUT-8(Ni) crystal structure viewed along [110] direction of the polymorph A (tetragonal) (a) and polymorph B (monoclinic) (b). $Ni_2(COO)_4$ paddle wheel unit is indicated by the red frame. $[Ni_2(ndc)_2]_n$ layers are indicated by a yellow frame. Dabco molecules connect the layers into 3D framework. The green arrows indicate the positions of metal-containing rows (blue frame). When viewed along the [110] direction, the metal-containing rows appear as layers, yet they also contain organic linkers oriented normally to the image plane. To prevent any confusion, we refer to them as "rows" (blue frame). Here, the crystallographic axis **c** runs along the rows. (c) A model of a disordered crystal as suggested in Ehrling et al., (2021). Ni in green, C in gray, O – in red. H atoms are omitted for clarity.

suspension of DUT-8(Ni) powder onto a carbon-coated copper grid and dried on air. TEM studies were performed using a Thermofisher TITAN TEM operated at 300 kV with an objective-side Cs-corrector, equipped with a Gatan Ultrascan 1000XP CCD camera.

2.3.1. TEM images

TEM images were collected at a nominal magnification of 69'000, at an electron dose of 11 e/Å^2. An objective aperture with a diameter of 100 μm, cutting reciprocal space information beyond 1.5 Å, was used. The TEM images were collected using a Digital Micrograph (GATAN, Pleasanton, USA) script, shifting the TEM stage in a regular grid, thus ensuring data collection from a fresh, previously unexposed area. A delay was built into the script after the stage shift before the exposure in order to minimize the stage-movement induced sample drift. The Digital Micrograph script is available at doi.org/10.5281/zenodo.12649027.

2.3.2. Diffraction patterns

Electron diffraction patterns were collected in nano-beam geometry using a 50 μm C2 condenser aperture and an electron beam of approximately 200 nm in diameter using the same Digital Micrograph (GATAN) script. The electron dose was 12.6 e/Å^2. After a diffraction pattern was collected, an image of the crystal was recorded by a second exposure. Second-shot images obtained at a nominal magnification of 27'000, after a diffraction pattern, were used to spot additional crystals in the illuminated area and to provide a low-resolution image for creating a mask support constraint in the phase retrieval procedure.

The data acquisition sequence was as follows: (1) recording the diffraction pattern; switching to imaging and (2) recording a low-resolution image of the crystal within the probe beam. As a result, for each sample, a pair of images was available for reconstruction - a diffraction pattern and a low-resolution image of the crystal.

Because of the high electron beam sensitivity of the sample, electron diffraction patterns later used for phase reconstruction and direct TEM images (nominal magnification of 69'000) could not be recorded from the same crystal. Consequently, direct comparisons between the structural features in a reconstructed image and those in a direct TEM image were not possible.

In the study, we used the complete diffraction patterns for reconstruction, as well as the central part of the diffraction pattern around the primary beam. In this context, we refer to the entire pattern as "high-resolution diffraction", while the central part is called "low-resolution diffraction data".

2.3.3. Characteristic electron dose

The resolution, both in images (via Fourier transformation) and in diffraction patterns, corresponds to the highest observed frequency. As longer exposures are used, lattice damage propagates, causing a shift of the highest visible frequency to lower scattering angles. The *critical* or *characteristic* electron dose D_c is defined as the dose at which a diffraction peak is reduced by a factor of e (2.72) (corresponding to 37 % reduction) of its initial value (Egerton, 2012). Consequently, each resolution shell can be associated with its own characteristic electron dose.

The characteristic electron dose D_c of the material was measured from a series of diffraction patterns acquired sequentially from the same sample area with the dose rate of 0.07 e/Å^{2}s. The estimated D_c was 2.5 e/Å^2 for 2 Å reflections, 7.7 e/Å^2 for 3 Å reflections, and 9.8 e/Å^2 for 4 Å reflections.

Electron diffraction patterns were simulated in eMAP software (AnaliTex, Stockholm, Sweden).

2.4. Computational details

The distribution of the projected potential was calculated as follows (Latychevskaia et al., 2022). The input data consisted of an array of the coordinates of all the atoms (x_n, y_n). The transmission function of a monolayer was calculated as: $t(x,y) = \exp[i\sigma v_z(x,y) \otimes l(x,y)]$, where $v_z(x,y)$ is the projected potential of an individual atom, $l(x,y)$ is the function describing positions of the atoms in the lattice, and $\otimes$ denotes convolution. The projected potential of a single atom was simulated as $v_z(r) = 4\pi^2 a_0 e \sum_{i=1}^{3} a_i K_0\left(2\pi r\sqrt{b_i}\right) + 2\pi a_0 e \sum_{n=1}^{3} \frac{c_i}{d_i} \exp\left(-\pi^2 r^2/d_i\right)$, where $r = \sqrt{x^2+y^2}$, a_0 is the Bohr radius, e is the elementary charge, $K_0(\ldots)$ is the modified Bessel function, and a_i, b_i, c_i, d_i are parameters tabulated elsewhere (Kirkland, 2010). In $v_z(r)$, The convolution $v_z(x,y) \otimes l(x,y)$ was calculated as $\mathrm{FT}^{-1}\{\mathrm{FT}[v_z(x,y)]\mathrm{FT}[l(x,y)]\}$, where FT and FT^{-1} stand for Fourier and inverse Fourier transforms, respectively. $\mathrm{FT}[l(x,y)]$ was calculated as a digital summation $\sum_n \exp\left[-i\left(k_x x_n + k_y y_n\right)\right]$, where (x_n, y_n) are the exact atomic coordinates. $\mathrm{FT}^{-1}\{\mathrm{FT}[v_z(x,y)]\mathrm{FT}[l(x,y)]\}$ was calculated by applying an inverse FFT to the product of $\mathrm{FT}[v_z(x,y)]$ and $\mathrm{FT}[l(x,y)]$.

3. Results

3.1. Imaging

Investigated DUT-8(Ni) MOF nanocrystals had a rectangular shape with well-developed {001} and {110} facets. No {100} or {010} facets were observed, which is dictated by the crystal structure – (001) and (110) planes form smooth, relatively densely packed terminal surfaces (see Fig. 1). Following the nanocrystal morphology, crystals were found to be oriented with $< 001 >$ and $< 110 >$ along the incident beam direction. We were primarily interested in the $< 110 >$ orientation, as the disorder in the structure could be best seen here (Fig. 1).

A direct image of a DUT-8(Ni) MOF nanocrystal is shown in Fig. 2a. This crystal is oriented with its $< 110 >$ direction orthogonal to the grid plane. The Fourier transform of the image is shown in Fig. 2b. Here, the elongation of reflections along the $< 110 >$ direction, associated with the crystal lattice disorder, is visible (Fig. 2b insert).

The peak at the highest resolution seen in the Fourier transform of the image corresponds to 330 (Fig. 2b) Bragg reflection with the interplanar d spacing of 4.34 Å. A simulated electron diffraction pattern of the $< 110 >$ zone, matching the orientation of the crystal, is shown in Fig. 2c. The electron dose applied during the collection of the TEM images was 11 e/Å^2. Thus, the minimal interplanar spacing observed matches well the resolution shell corresponding to the characteristic dose of over 10 e/Å^2 (Section 2.3.3).

Lattice fringes, associated with the distance between the Ni-containing rows, are clearly seen in the image (Fig. 2a), but neither the information on the nickel atoms' positions within the rows nor the linkers' positions can be distinguished.

3.2. Iterative reconstruction

3.2.1. Low-resolution reconstruction

For CDI reconstructions, images were acquired in pairs – first, an electron diffraction pattern, then, as a second exposure, an image of the crystal, as shown in Fig. 3a and Fig. 3b. During the acquisition of both the diffraction pattern and the image, the sample was illuminated by the same probing beam, only the projective lens parameters were changed. Thus, the second, direct image allowed judging whether the diffraction pattern was recorded from a single crystal and how well the crystal was centered within the beam. The crystal image in Fig. 4b exhibits concentric fringes due to Fresnel diffraction at the exit condenser aperture, which are irrelevant for the reconstruction routine because only the crystal shape was used later as a masking support.

The primary characteristic of the magnified central region in the diffraction pattern (Fig. 3c) is the vertical elongated area caused by detector overexposure. Additionally, two orthogonal bright stripes with modulations are evident. This is a typical diffraction pattern for a rectangular aperture. From the periods of these intensity modulations, the lateral crystal size dimensions can be deduced.

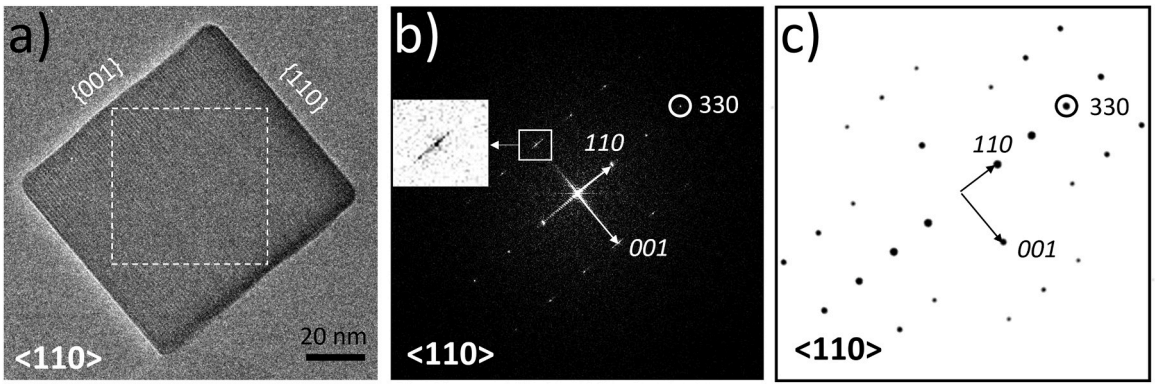

Fig. 2. TEM image of DUT-8(Ni) MOF nanocrystals (total dose 11 e/Å^2) oriented along < 110 > direction (a), corresponding Fourier transform taken from the dashed marked square area in Fig. 2a, is shown in (b). The white circle marks the 330 reflection – the highest-resolution Bragg spot seen in the image (b); and a simulated electron diffraction pattern in < 110 > direction (c). For the simulation, the regular polymorph A (tetragonal) structure (CSD 1989709) was used. Elongated reflections due to crystal lattice disorder are shown in the insert in (b).

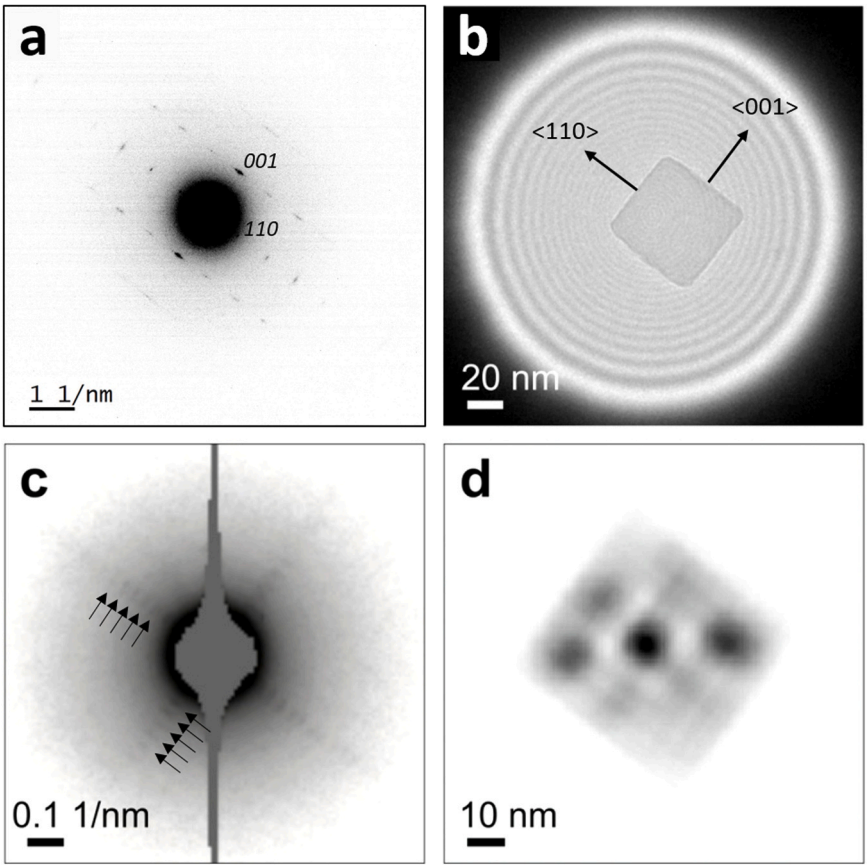

Fig. 3. Electron diffraction pattern of DUT-8(Ni) crystals. (a) Experimental electron diffraction pattern (intensity inverted), and (b) the corresponding image of the crystal within the electron beam (second exposure image). Note that the image of the crystal appears to be in focus, the concentric fringes around the nanocrystal are due to Fresnel diffraction at the exit aperture edges. (c) Magnified central region of the diffraction pattern shown in (a). Intensity oscillations due to the crystal shape are marked by groups of arrows. (d) The shape of the crystal as the amplitude distribution reconstructed from the diffraction pattern shown in (c) by iterative phase retrieval. The blurry spots inside the reconstructed crystal in (d) are artifacts due to the extended region of missing signal in the centre of the diffraction pattern (c). The crystal is aligned with < 110 > along the incident electron beam.

The crystal shape was reconstructed by applying iterative phase reconstruction to the central (low-resolution) part of the diffraction pattern (Fig. 3c). The overexposed area was masked out. The background signal was obtained by interpolating the signal between the four "cross" lines and then subtracted. The diffraction pattern was symmetrised as follows: $I_{\mathrm{sym}}\left(q_x, q_y\right) = \left[I\left(q_x, q_y\right) + I\left(-q_x, -q_y\right)\right]/2$. This procedure represents inversion symmetry averaging of Friedel pairs, being a legitimate approach for electron diffraction patterns recorded with very short wavelength and, therefore, an almost flat Ewald sphere. The symmetrization also neglects the possible intensity mismatch between Friedel pairs caused by dynamical scattering. We can argue that the crystals used in this study are sufficiently thin for this effect to be neglected, but we must acknowledge that the consequences of ignoring

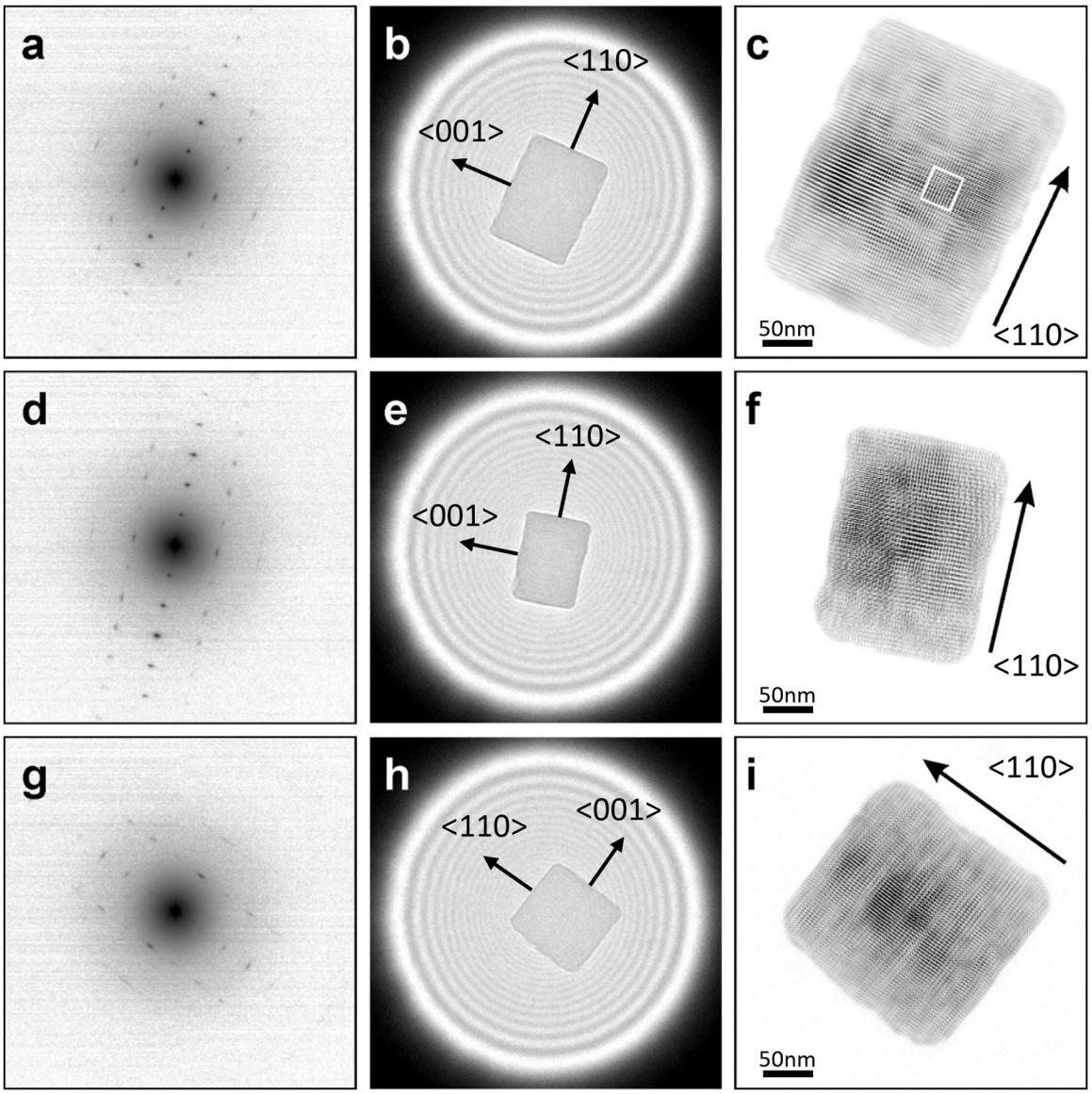

Fig. 4. Reconstruction images of DUT-8(Ni) MOF nanocrystals: (a), (d) and (g) experimental electron diffraction patterns, (b), (e) and (h) direct TEM images of the nanocrystals. (c), (f), (i) reconstructions. All crystals are oriented with $< 110 >$ along the incident electron beam. The arrows in the reconstructions indicate the $< 110 >$ crystallographic direction, corresponding to the stacking direction of Ni-dabco containing rows (see Fig. 1). The area marked by a white rectangle in (c) is later used for structure interpretation in 3.3.

Friedel pair differences are uncertain. A thorough analysis of this issue is beyond the scope of the manuscript.

The crystal shape was reconstructed from the obtained diffraction pattern by applying the hybrid input-output (HIO) algorithm (Fienup, 1982). In real space, the constraint of masking support was applied, where the mask was selected in the form of a perfect rectangular mask with dimensions obtained from the periods of the modulations. In the Fourier domain, the missing amplitudes blocked by the overexposed area were updated at each iteration during iterative phase retrieval (Latychevskaia, 2018). 200 iterative runs were made, each for 2000 iterations. The error was calculated by Miao et al. (1998, 2001); Miao and Sayre (2000):

$$\text{Error}_{f_k} = \left\{ \frac{\sum_{x,y \notin \gamma} |g'_k(x,y)|^2}{\sum_{x,y \in \gamma} |g'_k(x,y)|^2} \right\}^{1/2}. \quad (3)$$

From 200 obtained reconstructions, 20 reconstructions with the least error were selected, aligned, and averaged; the resulting reconstruction is shown in Fig. 3d. The reconstructed nanocrystal shape matches that recorded in the TEM image, reproducing well the irregular shape of edges and the smoothed corners. It should be noted that the irregularities of the reconstructed shape obtained are only due to the retrieved sample structure and not due to the reconstruction procedure, because the masking support had a perfect rectangular shape. The blurry, dark spots inside the crystals are artifacts, typically appearing when an object of constant amplitude is recovered from its diffraction pattern with a significant region of missing signal in the centre.

3.2.2. *High-resolution reconstruction*

The nanocrystal was imaged so that the conditions for iterative phase retrieval were fulfilled: there was only one nanocrystal in the probed region (Fig. 3b), and the size of the crystal was at least twice smaller than the size of the area not occupied by the crystal (oversampling condition). Additionally, the low-resolution shape of the crystal was available from the crystal image acquired in a second exposure (Section 3.2.1).

The reconstruction of the sample from its experimental diffraction pattern was achieved by applying HIO and error-reduction (ER) iterative

phase retrieval algorithms in alternating fashion, with 10 iterations each, starting with the HIO algorithm, 200 iterations in total. The constraints were applied as follows. In the sample plane, the sample distribution was assumed to be real positive, and a tight mask support from a real space image was applied.

In the detector plane, the amplitude was set to the square root of the intensity distribution with a loose mask selecting the peaks, the amplitude in the blocked centre region was updated during the iterative reconstruction. The initial phase in the detector plane was assumed to be random. 100 reconstructions were obtained for each sample. The results shown in Fig. 4 are the obtained reconstructions, which exhibited the least error, as calculated by Eq. (3).

Experimental electron diffraction patterns used for the image reconstruction are shown in Fig. 4a, d, g. The apparent resolution of the data is much higher here than in the TEM image shown in Fig. 2: reflections of the fifth order are clearly seen along the 110 direction, corresponding to 2.6 Å resolution; in the diagonal direction, even higher-resolution reflections are seen.

Iteratively reconstructed images do not represent an ultimately correct model of the structure, being rather a high-probability representation of the structure. The reconstructed images clearly show nickel-containing rows (orthogonal to <110 >). In some areas, the groups of nickel atoms within the rows can be recognized. This, in principle, could allow for a local determination of the stacking sequence. A diffraction pattern with sharp, distinct Bragg peaks would result in the reconstructed model that exhibits a regular lattice with atoms aligned along a certain direction. Additionally to Bragg peaks, the diffraction patterns of DUT-8(Ni) nanocrystals exhibit diffuse scattering lines associated with deviations of the sample structure from a perfect idealized lattice. The diffuse scattering shows up in the reconstruction as contrast variations within the nickel-containing rows. Our interpretation of the structural features observed in the reconstructed images, as nickel-containing rows and groups of atoms within these rows, suggests that the obtained image is a sensible representation of the structure.

With the contemporary possibilities of automation of TEM experiments, the task of electron diffraction data collection, suitable for iterative phase retrieval, should be easily achievable. The crucial points are the preparation of the sample with well-separated nanocrystals on the TEM grid and the post-processing of a large number of diffraction pattern / image pairs. The crystal images recorded as a second exposure allow for a simple judgment of the suitability of the pattern for the reconstruction (the placement of the crystal within the electron beam and the presence of the additional crystals) and can be used as a real space constraint.

3.3. Interpretation of the reconstructed images

Reconstructed images of three MOF nanocrystals are shown in Fig. 4c, f, i. Here, lattice fringes associated with the metal-containing rows are clearly seen. These rows are stacked orthogonal to the < 110 > direction (as marked by arrows in Fig. 4c,f,i).

Simulated projected potential for two regular structures – polymorph A (tetragonal) and polymorph B (monoclinic) (see Fig. 1a,b,) - viewed along < 110 > direction are shown in Fig. 5a and b. These images represent the ideal contrast of the crystalline lattices in the absence of disorder, noise, and instrumental errors. Fig. 5c shows an enlarged central section of the reconstructed image shown in Fig. 4c.

In the reconstructed image (Fig. 5c), the horizontal lines demonstrating the highest contrast were assigned to metal-containing rows (one of these rows is marked by a dashed blue line in Fig. 5c and a blue frame in Fig. 1b). Within these rows, clearly resolved maxima of intensity are observed. These maxima can be interpreted as the positions of nickel dimers within a paddle wheel building unit, matching the high-contrast areas in the projected potential of the regular structures (Figs. 5a, 5b). The rows are stacked in such a way that the metal-containing paddle wheel units lie almost above each other, following a line (red line in Fig. 5c), almost orthogonal to the direction of the rows (blue dashed line). This situation is realized in the polymorph A (tetragonal) of DUT-8(Ni), see Fig. 5a. We therefore conclude that in this area of the crystal, regular tetragonal stacking dominates. Nickel-containing paddle wheel units, lying above each other, are marked by red ellipses (Fig. 5c). The ellipse on the top of the region (marked white in Fig. 5c) is slightly shifted to the right from the straight line, suggesting that there is a shift of the nickel-containing group as a result of the crystal disorder. This shift is smaller than that expected for a regular monoclinic structure (Fig. 5b), which could easily be explained by the smaller shifts observed in the disordered model (Fig. 1c).

Significant intensity variations are observed between the rows, which can be assigned to the positions of organic ndc^{2-} linkers. Yet the contrast in these regions is smeared, so that no direct interpretation is possible.

4. Discussion

DUT-8 (Ni) nanocrystals were selected for this analysis primarily due to their morphology, which consists of small, isolated crystals with well-defined facets. This allows images and diffraction patterns to be recorded with a probe beam size that ensures the field of view is at least twice the size of the crystals (oversampling condition) (Miao et al., 1998). Additionally, the crystals are sufficiently small to produce

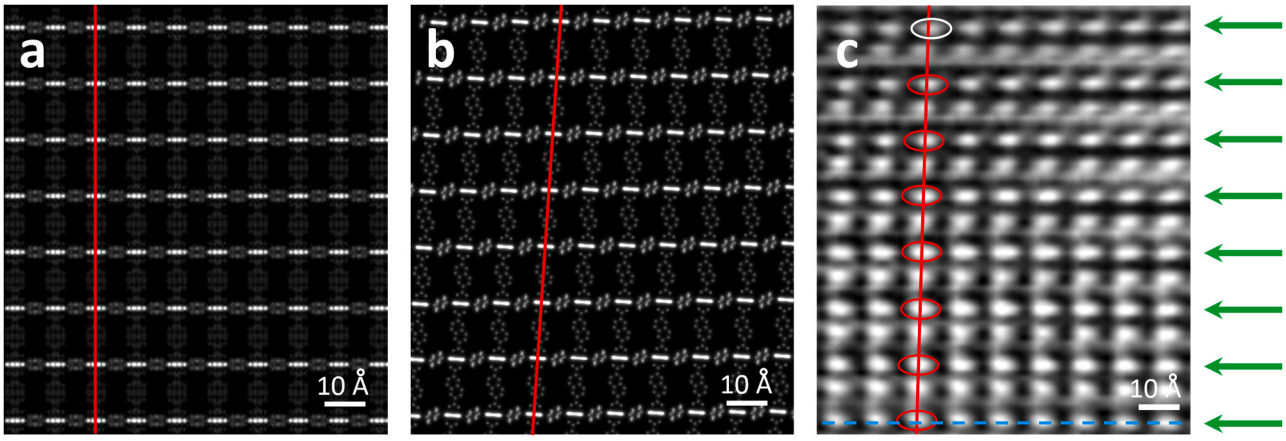

Fig. 5. Simulated projected potential of the polymorph A (tetragonal) (a) and polymorph B (monoclinic) (b) for DUT-8(Ni) MOF structure viewed along < 110 > direction; (c) enlarged central section of the reconstructed image shown in Fig. 4c. Green arrows indicate nickel-containing rows; the distance between the rows is 13 Å.

low-resolution diffraction patterns based on their overall shape. To the best of our knowledge, this is the first direct observation of the crystal shape effect in electron diffraction.

The electron diffraction patterns obtained from DUT-8(Ni) MOF nanocrystals revealed distinct features at both low and high resolutions. Low-resolution features were associated with the crystal shape, while high-resolution details (beyond 2.6 Å) provided insights into the material's crystalline structure. These two regions were separated, enabling separate coherent diffraction imaging (CDI) analyses.

The reconstruction from low-resolution data accurately depicted the crystal shape, albeit with a blurred contrast due to the extended overexposed area of the primary beam. Implementing a detector with a higher dynamic range could mitigate this effect and potentially enhance the quality of the reconstructed crystal image.

The reconstruction from high-resolution diffraction data yielded images with meaningful contrast, which could be interpreted on the basis of structural features. The high-resolution reconstruction procedure used the information on the crystal image as a real space constraint. In principle, the low-resolution reconstructed image of the crystal shape could serve as this constraint, particularly if recorded with a proper detector. Thus, this approach presents a pathway for image reconstruction based solely on diffraction data, eliminating the need for additional direct-space images. Although the subsequent image is not necessary, it is helpful for ensuring that there was a single object in the field of view.

We should note that the resolution of the reconstructed image, corresponding to the resolution of the diffraction data used, was 2.6 Å. In contrast, a direct lattice image recorded at a similar total dose had a resolution of 4.34 Å. This comparison indicates a 1.7-fold increase in information content achieved through CDI reconstruction. Additionally, we did not utilize state-of-the-art high-resolution TEM (HR-TEM) with modern detectors. Our primary goal was to demonstrate the feasibility of reconstructing the crystal structure solely from diffraction patterns and to show that this approach can operate under electron dose conditions that are milder, potentially enabling higher-resolution reconstructions than traditional direct imaging.

While modern hybrid detectors provide the capability to record data with a very high dynamic range (Zambon et al., 2023), enabling analysis of the primary electron beam's shape, the current technology falls short in allowing for large-area detectors with seamlessly integrated chips. This limitation poses a challenge when requiring well-recorded data (without gaps) at both low and high resolutions. We hope that this technical challenge will be addressed in future advancements, allowing for a full CDI reconstruction to be possible from a single diffraction pattern.

5. Conclusions

We have successfully demonstrated the iterative reconstruction of DUT-8(Ni) MOF nanocrystals. In addition to capturing high-resolution diffraction features associated with the crystal structure, the crystals exhibited oscillations in the low-resolution region near the primary beam, reflecting the distinct crystal shape. Consequently, we segregated the information from these two resolution regions and conducted separate reconstruction processes for the crystal shape and crystal structure.

Both types of reconstructed images revealed contrast features that could be well interpreted. The low-resolution reconstruction generated images depicting the crystal shape. Despite being affected by artifact contrasts, it faithfully reproduced the crystal shape. The high-resolution image reconstruction provided images with interpretable contrast based on the structure of DUT-8(Ni): the nickel-containing clusters were well resolved, and the shifts in rows could be interpreted in light of the complex disorder in the system. The contrast features in the linker areas were less interpretable, likely due to beam damage and the intricacies of the disordered structure.

Funding

This work was supported by the German Research Foundation projected CRC 1279, CRC 1415 (417590517), and FOR 2433 (279409724), and Swiss National Research Foundation grants 200021_197107 and 10003659.

CRediT authorship contribution statement

Ute Kaiser: Writing – review & editing. **Mariia Maliuta:** Investigation. **Stefan Kaskel:** Writing – review & editing. **Tatiana E. Gorelik:** Writing – review & editing, Writing – original draft, Methodology, Investigation, Formal analysis, Conceptualization. **Tatiana Latychevskaia:** Writing – review & editing, Writing – original draft, Methodology, Investigation, Formal analysis, Conceptualization. **Irena Senkovska:** Writing – original draft, Investigation.

Declaration of Competing Interest

The authors declare that they have no known competing financial interests or personal relationships that could have appeared to influence the work reported in this paper.

Acknowledgments

The authors are grateful to Andrew Goodwin (University of Oxford, UK) for providing the model of disordered DUT-8(Ni).

Data availability

Data will be made available on request.

References

Bon, V., Klein, N., Senkovska, I., Heerwig, A., Getzschmann, J., Wallacher, D., Zizak, I., Brzhezinskaya, M., Mueller, U., Kaskel, S., 2015. Exceptional adsorption-induced cluster and network deformation in the flexible metal–organic framework DUT-8(Ni) observed by in situ X-ray diffraction and EXAFS. Phys. Chem. Chem. Phys. 17, 17471–17479.

Egerton, R.F., 2012. Mechanisms of radiation damage in beam-sensitive specimens, for TEM accelerating voltages between 10 and 300 kV. Microsc. Res. Tech. 75, 1550–1556.

Ehrling, S., Reynolds, E.M., Bon, V., Senkovska, I., Gorelik, T.E., Evans, J.D., Rauche, M., Mendt, M., Weiss, M.S., Pöppl, A., Brunner, E., Kaiser, U., Goodwin, A.L., Kaskel, S., 2021. Adaptive response of a metal-organic framework through reversible disorder-disorder transitions. Nat. Chem. 13, 568–574.

Fienup, J.R., 1982. Phase retrieval algorithms: a comparison. Appl. Opt. 21, 2758–2769.

Gerchberg, R.W., Saxton, W.O., 1972. A practical algorithm for the determination of phase from image and diffraction plane pictures. Optik 35, 237–246. *Optik*, **35**, 237-246.

Horike, S., Shimomura, S., Kitagawa, S., 2009. Soft porous crystals. Nat. Chem. 1, 695–704.

Jiang, Y., Chen, Z., Han, Y., Deb, P., Gao, H., Xie, S., Purohit, P., Tate, M.W., Park, J., Gruner, S.M., Elser, V., Muller, D.A., 2018. Electron ptychography of 2D materials to deep sub-ångström resolution. Nature 559, 343–349.

Kavoosi, N., Bon, V., Senkovska, I., Krause, S., Atzori, C., Bonino, F., Pallmann, J., Paasch, S., Brunner, E., Kaskel, S., 2017. Tailoring adsorption induced phase transitions in the pillared-layer type metal–organic framework DUT-8(Ni). Dalton Trans. 46, 4685–4695.

Kirkland, E.J., 2010. Advanced Computing in Electron Microscopy. Springer.

Klein, N., Herzog, C., Sabo, M., Senkovska, I., Getzschmann, J., Paasch, S., Lohe, M.R., Brunner, E., Kaskel, S., 2010. Monitoring adsorption-induced switching by 129Xe NMR spectroscopy in a new metal–organic framework $Ni_2(2,6\text{-ndc})_2(dabco)$. Phys. Chem. Chem. Phys. 12, 11778–11784.

Krause, S., Hosono, N., Kitagawa, S., 2020. Chemistry of soft porous crystals: structural dynamics and gas adsorption properties. Angew. Chem. Int. Ed. 59, 15325–15341.

Latychevskaia, T., 2018. Iterative phase retrieval in coherent diffractive imaging: practical issues. Appl. Opt. 57, 7187–7197.

Latychevskaia, T., Huang, P., Novoselov, K.S., 2022. Imaging defects in two-dimensional crystals by convergent-beam electron diffraction. Phys. Rev. B 105, 184113.

Latychevskaia, T., Longchamp, J.-N., Fink, H.-W., 2012. When holography meets coherent diffraction imaging. Opt. Express 20, 28871–28892.

Li, Y., Wang, K., Zhou, W., Li, Y., Vila, R., Huang, W., Wang, H., Chen, G., Wu, G.-H., Tsao, Y., Wang, H., Sinclair, S., Chiu, W., Cui, Y., 2019. Cryo-EM structures of atomic surfaces and host-guest chemistry in metal-organic frameworks. Matter 1, 428–438.

Liu, L., Chen, Z., Wang, J., Zhang, D., Zhu, Y., Ling, S., Huang, K.-W., Belmabkhout, Y., Adil, K., Zhang, Y., Slater, B., Eddaoudi, M., Han, Y., 2019. Imaging defects and their evolution in a metal-organic framework at sub-unit-cell resolution. Nat. Chem. 11, 622–628.

Liu, L., Zhang, D., Zhu, Y., Han, Y., 2020. Bulk and local structures of metal–organic frameworks unraveled by high-resolution electron microscopy. Commun. Chem. 3, 99.

Marchesini, S., He, H., Chapman, H.N., Hau-Riege, S.P., Noy, A., Howells, M.R., Weierstall, U., Spence, J.C.H., 2003. X-ray image reconstruction from a diffraction pattern alone. Phys. Rev. B 68 (R), 140101.

Miao, J.W., Charalambous, P., Kirz, J., Sayre, D., 1999. Extending the methodology of X-ray crystallography to allow imaging of micrometre-sized non-crystalline specimens. Nature 400, 342–344.

Miao, J.W., Hodgson, K.O., Sayre, D., 2001. An approach to three-dimensional structures of biomolecules by using single-molecule diffraction images. Proc. Natl. Acad. Sci. USA 98, 6641–6645.

Miao, J.W., Sayre, D., 2000. On possible extensions of X-ray crystallography through diffraction-pattern oversampling. Acta Crystallogr. A 56, 596–605.

Miao, J.W., Sayre, D., Chapman, H.N., 1998. Phase retrieval from the magnitude of the Fourier transforms of nonperiodic objects. J. Opt. Soc. Am. A 15, 1662–1669.

Parent, L.R., Pham, C.H., Patterson, J.P., Denny, M.S., Cohen, S.M., Gianneschi, N.C., Paesani, F., 2017. Pore breathing of metal-organic frameworks by environmental transmission electron microscopy. JACS 139, 13973–13976.

Petkov, P.S., Bon, V., Hobday, C.L., Kuc, A.B., Melix, P., Kaskel, S., Düren, T., Heine, T., 2019. Conformational isomerism controls collective flexibility in metal–organic framework DUT-8(Ni). Phys. Chem. Chem. Phys. 21, 674–680.

Schneemann, A., Bon, V., Schwedler, I., Senkovska, I., Kaskel, S., Fischer, R.A., 2014. Flexible metal–organic frameworks. Chem. Soc. Rev. 43, 6062–6096.

Senkovska, I., Bon, V., Abylgazina, L., Mendt, M., Berger, J., Kieslich, G., Petkov, P., Luiz Fiorio, J., Joswig, J.-O., Heine, T., Schaper, L., Bachetzky, C., Schmid, R., Fischer, R. A., Pöppl, A., Brunner, E., Kaskel, S., 2023. Understanding MOF flexibility: an analysis focused on pillared layer MOFs as a model system. Angew. Chem. Int. Ed. 62, e202218076.

Wiktor, C., Meledina, M., Turner, S., Lebedev, O.I., Fischer, R.A., 2017. Transmission electron microscopy on metal–organic frameworks – a review. J. Mater. Chem. A 5, 14969–14989.

Kaskel, S. (Ed.), 2016. The Chemistry of Metal-Organic Frameworks: Synthesis, Characterization, and Applications. Wiley.

Wu, J.S., Weierstall, U., Spence, J.C.H., 2005. Diffractive electron imaging of nanoparticles on a substrate. Nat. Mater. 4, 912–916. The paper was retracted in 2006: the image solution was not unique, the substrate scattering was incorrectly treated.

Zambon, P., Vávra, J., Montemurro, G., Bottinelli, S., Dudina, A., Schnyder, R., Hörmann, C., Meffert, M., Schulze-Briese, C., Stroppa, D., Lehmann, N., Piazza, L., 2023. High-frame rate and high-count rate hybrid pixel detector for 4D STEM applications. Front. Phys. 11. https://doi.org/10.3389/fphy.2023.1308321.

Zhou, L., Song, J., Kim, J.S., Pei, X., Huang, C., Boyce, M., Mendonça, L., Clare, D., Siebert, A., Allen, C.S., Liberti, E., Stuart, D., Pan, X., Nellist, P.D., Zhang, P., Kirkland, A.I., Wang, P., 2020. Low-dose phase retrieval of biological specimens using cryo-electron ptychography. Nat. Commun. 11, 2773.

Zuo, J.M., Vartanyants, I., Gao, M., Zhang, R., Nagahara, L.A., 2003. Atomic resolution imaging of a carbon nanotube from diffraction intensities. Science 300, 1419–1421.